LETTER

https://doi.org/10.1038/s41586-019-1010-0

Deep electrical imaging of the ultraslow-spreading Mohns Ridge

Ståle Emil Johansen[1]*, Martin Panzner[2], Rune Mittet[2], Hans E. F. Amundsen[3], Anna Lim[1], Eirik Vik[1], Martin Landrø[4] & Børge Arntsen[1]

More than a third of mid-ocean ridges have a spreading rate of less than 20 millimetres a year[1]. The lack of deep imaging data means that factors controlling melting and mantle upwelling[2,3], the depth to the lithosphere–asthenosphere boundary (LAB)[4,5], crustal thickness[6–9] and hydrothermal venting are not well understood for ultraslow-spreading ridges[10,11]. Modern electromagnetic data have greatly improved our understanding of fast-spreading ridges[12,13], but have not been available for the ultraslow-spreading ridges. Here we present a detailed 120-kilometre-deep electromagnetic joint inversion model for the ultraslow-spreading Mohns Ridge, combining controlled source electromagnetic and magnetotelluric data. Inversion images show mantle upwelling focused along a narrow, oblique and strongly asymmetric zone coinciding with asymmetric surface uplift. Although the upwelling pattern shows several of the characteristics of a dynamic system[3,12–14], it probably reflects passive upwelling controlled by slow and asymmetric plate movements instead. Upwelling asthenosphere and melt can be traced to the inferred depth of the Mohorovičić discontinuity and are enveloped by the resistivity (100 ohm metres) contour denoted the electrical LAB (eLAB). The eLAB may represent a rheological boundary defined by a minimum melt content. We also find that neither the melt-suppression model[7] nor the inhibited-migration model[15], which explain the correlation between spreading rate and crustal thickness[6,16–19], can explain the thin crust below the ridge. A model in which crustal thickness is directly controlled by the melt-producing rock volumes created by the separating plates is more likely. Active melt emplacement into oceanic crust about three kilometres thick culminates in an inferred crustal magma chamber draped by fluid convection cells emanating at the Loki's Castle hydrothermal black smoker field. Fluid convection extends for long lateral distances, exploiting high porosity at mid-crustal levels. The magnitude and long-lived nature of such plumbing systems could promote venting at ultraslow-spreading ridges.

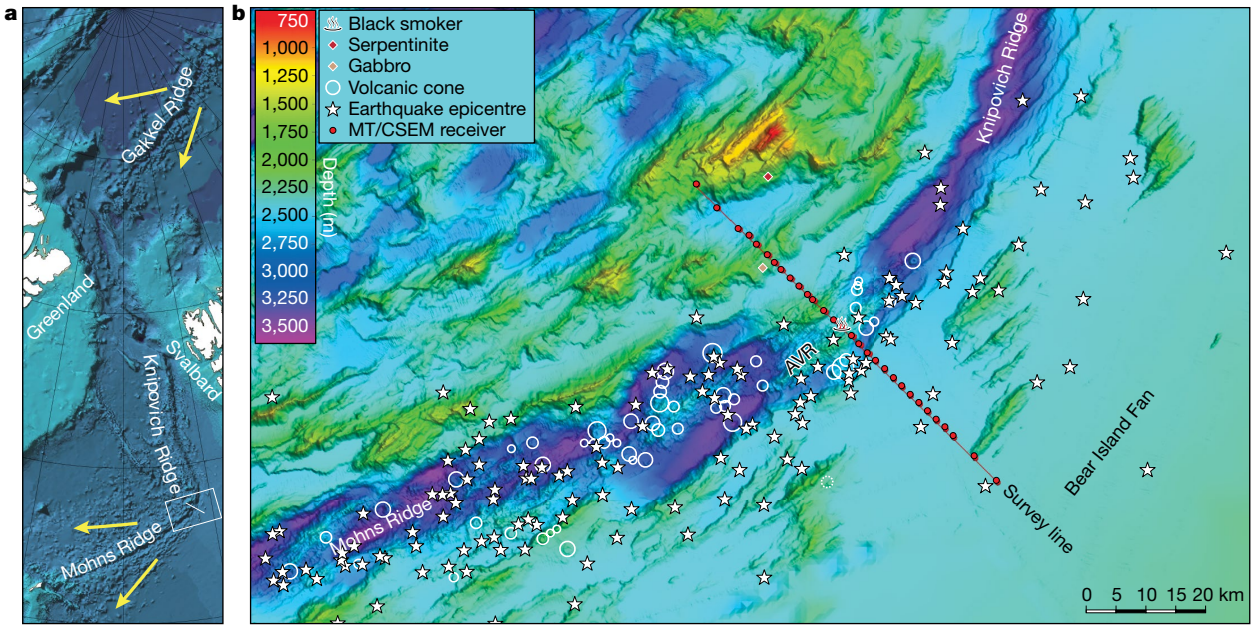

Fig. 1 | Location of the joint MT and CSEM survey across the ultraslow-spreading Mohns Ridge. a, Location of the Mohns, Knipovich and Gakkel ridges along the ultraslow-spreading Arctic mid-ocean ridge system[11] (https://commons.wikimedia.org/wiki/File:IBCAOver1map.jpg). Yellow arrows denote the plate movement of North America and Eurasia relative to a fixed hotspot reference frame[32]. The white rectangle (with line) marks the location of panel **b** (and the survey line). **b**, Layout of 30 MT and CSEM receivers across the Mohns Ridge (https://kartkatalog.geonorge.no/metadata/kartverket/dybdedata-radata/2fe7b56c-334d-4660-ac50-6fcf973a0f70). The black smoker vent field Loki's Castle is located at the crest of the axial volcanic ridge (AVR) at the centre of the survey line. White circles denote circular and conical features interpreted as seabed volcanoes. Serpentinite and gabbro outcrops sampled by dredging are marked with diamond symbols. Stars denote epicentres for earthquakes with moment magnitudes exceeding 4.0 in the time period 1990–2018 from the International Seismological Centre database. We note the regional asymmetry of the Mohns Ridge, with uplift of the western flank of the rift graben relative to the eastern margin partly covered in sediments from the Bear Island Fan. Earthquakes with moment magnitudes exceeding 4.0 are concentrated along the ridge graben and the southeastern ridge flank and are nearly absent along the western graben margin.

[1]Department of Geoscience and Petroleum, Norwegian University of Science and Technology (NTNU), Trondheim, Norway. [2]EMGS ASA, Trondheim, Norway. [3]Vestfonna Geophysical AS, Trondheim, Norway. [4]Department of Electronic Systems, Norwegian University of Science and Technology (NTNU), Trondheim, Norway. *e-mail: stale.johansen@ntnu.no

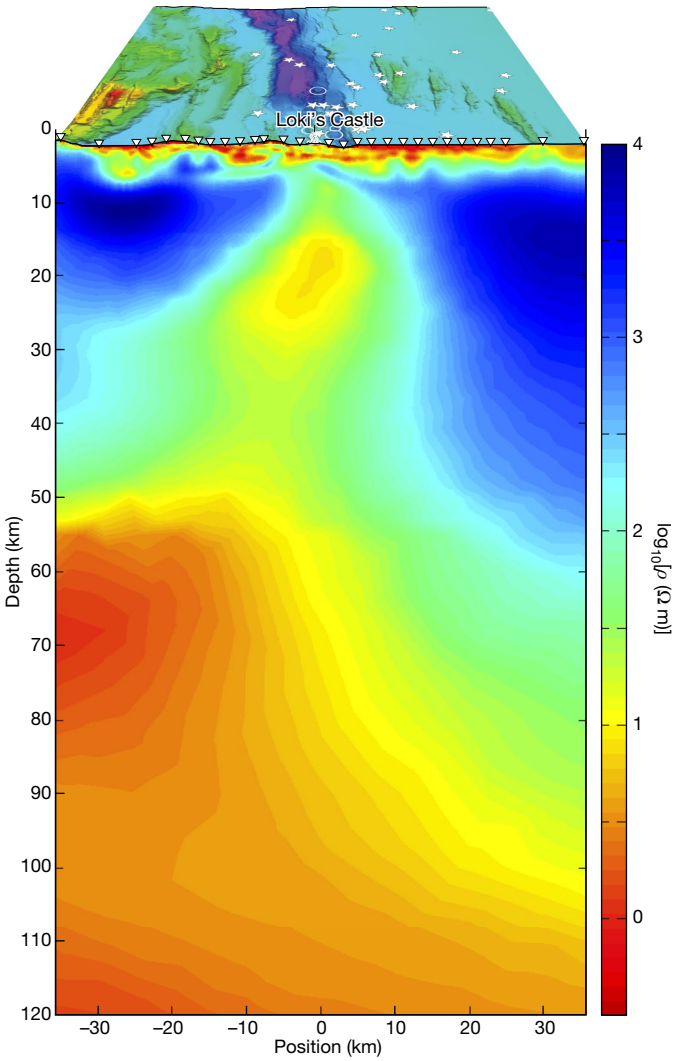

Fig. 2 | Joint MT and CSEM resistivity image of mantle upwelling beneath the ultraslow-spreading Mohns Ridge. Top panel, surface view of seafloor topography, seabed volcanoes and earthquake epicentres from Fig. 1b. In the main panel, colours show resistivity ρ_y in the horizontal inline direction obtained from joint nonlinear inversion of MT and CSEM data from receivers at the seafloor (inverted triangles). Full anisotropic resistivity results are shown in Extended Data Fig. 5.

The ultraslow-spreading ridges[1] are characterized by linked magmatic and amagmatic sections, mantle rocks at the sea floor, abundant hydrothermal venting and along-strike variations of lithospheric thickness, volcanism and earthquake activity[1,4,6,10,11,16]. For fast-spreading ridges especially, electromagnetic deep imaging has substantially improved understanding of structures and evolution[12,13], but this is not the case for the slowest-spreading ridges. Factors controlling decompression melting and mantle upwelling[2,3], the characteristics of and depth to the LAB[4,5], melt supply and crustal thickness[6–9] and hydrothermal venting[10,11] are still poorly known.

To map the ultraslow-spreading Arctic Mid-Ocean Ridge system we acquired both magnetotelluric (MT) and controlled source electromagnetic (CSEM) data across the Mohns Ridge. Data were collected by 30 electromagnetic seafloor receivers along a 68-km line transecting the active black smoker field Loki's Castle[11] (Fig. 1). Smooth two-dimensional anisotropic electrical resistivity models were reconstructed from the measured data using nonlinear regularized joint inversion of MT and CSEM data and individual inversion of the CSEM data[13,20].

The resistivity model from the joint inversion shows conductivity variations down to depths of 120 km (Fig. 2). The ridge axis is centred above a high-conductivity anomaly indicating mantle upwelling focused along a narrow, oblique and strongly asymmetric zone. When interpreting the two-dimensional conductivity sections and selected vertical profiles through the oceanic lithosphere (Figs. 2–4, Extended Data Fig. 6), the temperature, lithology, porosity, permeability, fluid content and melt content must be taken into account[21].

We interpret the contour at about 100 Ω m (the eLAB) to denote the base of the electrical lithosphere. This surface defines an envelope for mantle upwelling and melt migration rising to shallow levels beneath the ridge axis. Outside and above the eLAB there is a rapid transition to high resistivities typical of melt-free peridotite, and we assume that measured values coincide with the SEO3 conductivity-versus-temperature model for dry peridotite[22]. Figure 3a shows conductivity-versus-temperature models for dry peridotite, basalt and gabbro together with selected temperature-versus-resistivity profiles (west, axial, east) for the Mohns Ridge and the East Pacific Rise[13]. Selected profiles with corresponding geotherms and calculated partial melt content are shown in the temperature-versus-depth and resistivity-versus-depth domains in Extended Data Fig. 6. Figure 3b and Extended Data Fig. 6c show that the lithosphere beneath the eastern flank is much colder and thicker than predicted by halfspace cooling[23] with the eLAB occurring more than 30 km deeper than the predicted 1,300 °C thermal LAB. West of the ridge, the lithosphere beneath the western flank is thinner and warmer with inferred temperatures comparable to halfspace cooling (Fig. 3b, Extended Data Fig. 6a).

At depth the transition from the highly conductive melt-rich region is more abrupt to the west compared to the eastern side of the ridge. The western lithosphere also resembles a seismic shear wave velocity-versus-depth model estimated further south on the Mohns Ridge[24]. However, this model cannot reliably image east–west asymmetry since it is based on one-dimensional approximation and is dominated by events from the western side of the ridge.

High conductivities along the axial profile indicate a high melt content at depth (Fig. 3b, Extended Data Fig. 6e). However, when evaluating the highest values, it should be kept in mind that MT data is sensitive to the integrated conductance of conductive bodies. At depths of 20 km or so along the axial profile, the lava-lamp-shaped high-conductivity anomaly (Fig. 3b), bracketed by the 25 Ω m contour, is interpreted to reflect at least 1% melt content within the upwelling asthenosphere (Extended Data Fig. 6). Melt content decreases within the plume head with resistivities indicating less than 1% melt at the depth of the inferred Mohorovičić discontinuity. In Figs. 3b, 4 this surface is denoted the electrical Moho (eMoho) because it cannot be directly calibrated with the Mohorovičić discontinuity. Conductivities near the seafloor are close to that of seawater but decrease rapidly down through the crust, reflecting seawater infiltration and a decreasing porosity (Fig. 4).

Between depths of about 4 km and 5 km, rapidly increasing conductivities at temperatures above that of the dry basalt solidus suggest increasing melt content and could indicate a magma chamber at this level (Figs. 3a, 4c). Figure 4a shows fluid convection cells (the elongated and winding high-conductivity anomalies partly draping the inferred magma chamber and emanating at Loki's Castle).

Anisotropy is not important in the inverted models. An exception is the shallow zone below the ridge (Fig. 3b, Extended Data Fig. 5) indicating vertical transport also occurring via faults and fractures. Correlation between earthquake epicentres, faults and volcanoes at the graben floor (Figs. 1, 2) support interplay between melt emplacement and faulting.

The Mohns Ridge is asymmetric also at shallow levels (Figs. 1, 2). The western margin is uplifted relative to the eastern side (Figs. 1, 2, 3b, 4) and large negative relief and easterly dipping faults characterize the graben. The topography along the eMoho surface (Fig. 4) suggests that some faults extend into the upper mantle. Exposed serpentinite and gabbro have been dredged west of Loki's Castle[11,25] (Fig. 1) and the very shallow high-resistivity rocks in the western part of the CSEM section substantiate these observations (Fig. 4).

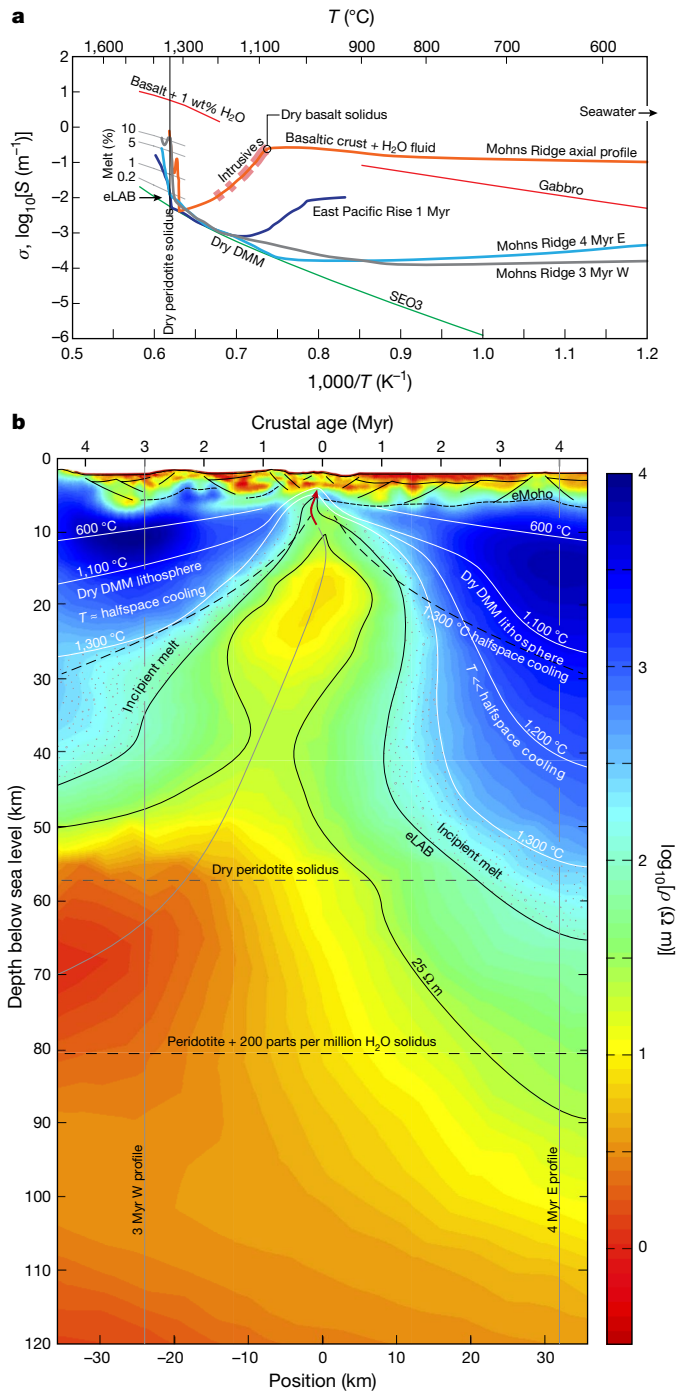

Fig. 3 | Conductivity and temperature versus depth and geometry of the lithosphere–asthenosphere boundary beneath the Mohns Ridge. **a**, Conductivity σ versus temperature T for selected profiles in panel **b** (3 Myr west, axial, 4 Myr east) using temperatures derived from the adiabatic and geothermal gradients illustrated in Extended Data Fig. 6. Conductivity versus temperature for a 1-Myr profile from the East Pacific Rise is shown for comparison[13]. The SEO3 conductivity-versus-temperature model for dry olivine[22] constrains the maximum temperature for any measured conductivity for dry depleted MORB mantle (dry DMM) indicating lower lithosphere temperatures that are substantially below the halfspace cooling both along the eastern segment of the Mohns Ridge and at the East Pacific Rise. Conductivity-versus-temperature profiles for DMM + 0.2%, 1%, 5% and 10% melt (basalt + 1 wt% H_2O) were calculated using the HS+ model[21]. Intrusives and basaltic crust + H_2O fluid annotated on the axial profile are outlined in detail in Fig. 4. The contour at 100 Ω m (0.01 $S\ m^{-1}$) marking the transition from upwelling asthenosphere to DMM lithosphere is denoted the eLAB. The dry peridotite solidus at 1,340 °C marks the intersection between adiabatic upwelling mantle with a potential temperature T_p of 1,315 °C and the dry peridotite solidus as is illustrated in Extended Data Fig. 6. **b**, Joint MT and CSEM resistivity image showing temperatures, the eLAB and the eMoho. On the top axis, crustal ages are relative to a half-spreading rate of 8 mm yr^{-1}. Estimated isotherms are displayed as white lines with the 1,300 °C halfspace cooling isotherm (dashed black line) shown for reference. Lithosphere temperatures for depths shallower than 15 km below the seabed are assumed to be similar to the halfspace cooling. The inferred Moho depth (eMoho) is taken from Fig. 4. The dry and 200 parts per million H_2O solidi for peridotite are taken from Extended Data Fig. 6 and ref. [42]. Incipient (less than 0.2 wt%) melt within the lithosphere bordering the eLAB is derived from modelling presented in Extended Data Fig. 6.

Geophysical studies suggest that crustal thicknesses[24,26–28] along the Mohns and Knipovich ridges are 2–5 km, noticeably below the global average[6,9] of around 7 km. However, such estimates are uncertain because the coupling between seismic and igneous 'crust' is not established for ultraslow-spreading ridges[8,9]. From the published geophysical results[24,26–28] and our CSEM observations (Fig. 4) we suggest an approximate crustal thickness, as indicated by the eMoho surface in Fig. 4. This surface probably represents a porosity threshold either within the lower-crustal gabbro sequence or at the transition from gabbro to peridotite lithologies at the base of the crust. The apparent eMoho/eLAB at 2.8 km beneath the ridge axis (Fig. 4c) suggests the latter.

The general view is that crustal thickness is dependent on spreading rate with thinner or no crust at ultraslow-spreading ridges[6,16–19]. In the melt suppression end-member model[7], convective cooling forms a thick thermal boundary layer (lid) below the ridge axis that shuts off melt production down to 30 km or deeper. In the other end-member model, melt production is normal, but a similar but much thinner lid hampers melt migration to the surface[15].

Deep convective cooling should form a thick low-resistivity layer (30 km) extending below the ridge. Our inversion images (Figs. 2–4) do not support such a model; instead the mantle structure is broken by an open and partly melted column rising from the asthenosphere. This column extends to shallow levels and it is difficult to include even a much thinner lid (about 7 km), as proposed by the other end-member model and as also suggested farther south on the Mohns Ridge[24].

When comparing the cross-sections from the ultraslow-spreading Mohns Ridge (Fig. 2) and the fast-spreading East Pacific Rise[13], the most notable difference between the two is not the development of lids below the ridges as predicted by the end-member models. Instead, it is the shape and size of the melt-prone areas. These observations suggest that an alternative model without a lid and a much more open and active melt conduit better explains the observations beneath Loki's Castle. In this model, spreading rate more directly controls the volume of partly melted upwelling asthenosphere and thereby the crustal thickness.

While melt content and high temperatures reduce resistivity at depth, we have interpreted the conductive patterns in the crust to be caused by convecting saline fluids (Fig. 4, Extended Data Fig. 4). The Loki's Castle vent field has fluid geochemistry indicating a sedimentary source area[29], and circulation patterns suggest drainage of sediment pore water from the Bjørnøya fan 10 km east of the ridge axis. The magnitude and long-lived nature of such plumbing systems could promote circulation and explain why ultraslow-spreading ridges often deviate from a linear relationship between spreading rate and venting[11,29].

Deviation between the selected resistivity-versus-depth profiles and the dry DMM SEO3 profile (Extended Data Fig. 6), in addition to a faulted eMoho surface, could indicate even deeper saline water infiltration. However, the smoothing penalty applied in the data inversion means that it is difficult to locate the exact position and nature of the transition from dry to wet lithologies. Infiltration of seawater causing extensive serpentinization[11] could explain the low seismicity at the graben margin west of Loki's Castle[4] (Figs. 1, 2).

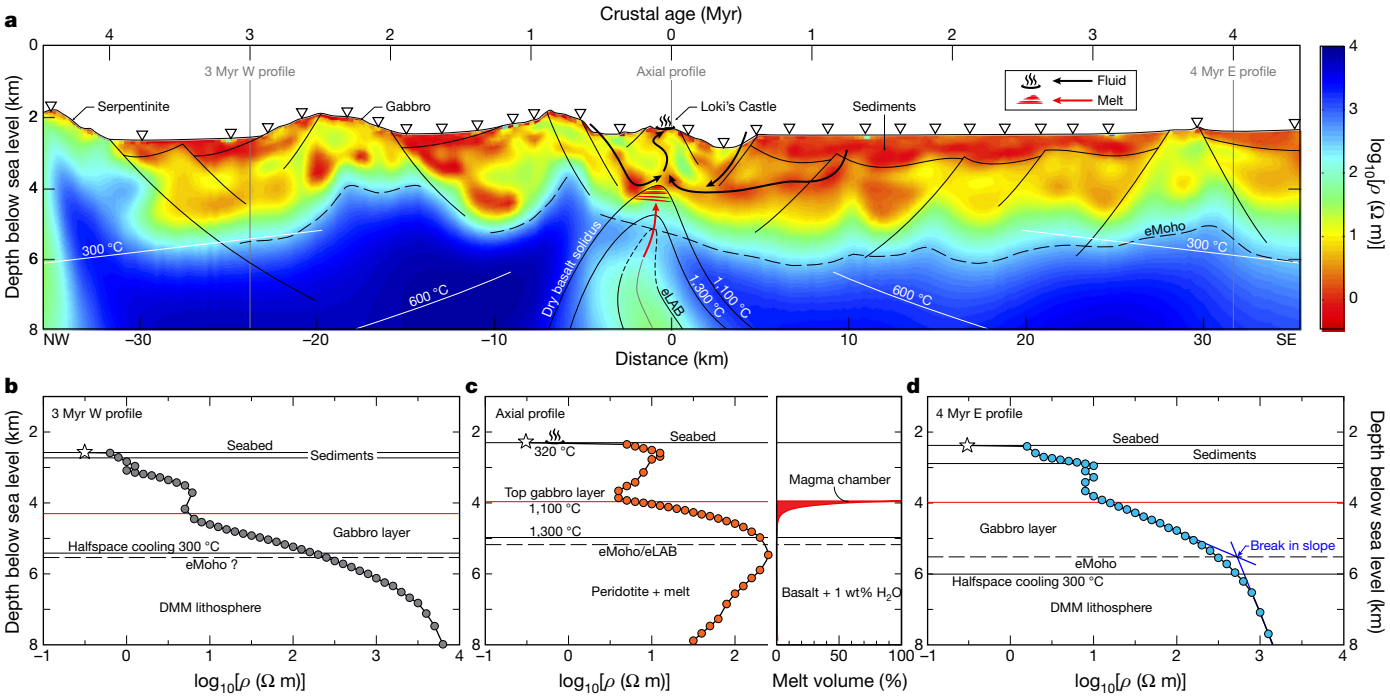

Fig. 4 | Inversion image of CSEM resistivity data across the ultraslow-spreading Mohns Ridge. a, The colours show resistivity ρ_h in the horizontal direction. Full anisotropic resistivity results from CSEM inversion are shown in Extended Data Fig. 4. The eLAB at 100 Ω m (Fig. 3) is derived from measured conductivities while the 1,300 °C and 1,100 °C isotherms are derived from a combination of measured conductivities and halfspace cooling model data with the dry basalt solidus straddling the 1,100 °C isotherm. The 300 °C and 600 °C isotherms represent halfspace cooling temperatures[23]. **b**, Measured resistivity versus depth for the 3 Myr west profile. A tentative top gabbro layer horizon is derived by comparison with panel **c**. **c**, Measured resistivity versus depth for the axial profile. Volume per cent melt (basalt + 1 wt% H_2O) was calculated using the HS+ model[21]. Increasing conductivities indicate a magma chamber at mid-crustal levels below the ridge, probably defining the top of the gabbro layer. **d**, Measured resistivity versus depth for the 4 Myr east profile. A tentative top gabbro layer horizon is derived by comparison with panel **c**. The marked break in slope for conductivity versus depth at about 3.2 km below the seabed represents a shift in porosity, indicating the transition from dominantly gabbroic to peridotite lithologies within the DMM lithosphere (eMoho).

Dynamic pressure gradients created by asthenospheric corner flow[30] or magma guiding along the base of the thermal lithosphere[31] are dominant hypotheses explaining melt focusing towards the ridge axis. In the fixed hotspot reference frame[32], the North American plate moves westwards while the Eurasian plate moves parallel to the ridge towards the southwest. This oblique and asymmetric spreading at Loki's Castle (Fig. 1a) produces large differences in orthogonal half-spreading rates. Because the corner flow model couples the size, width and shape of the melting zone to the spreading rate, the asymmetric spreading could potentially also create the observed asymmetric melting zone below the ridge (Fig. 2). Focusing of melt could be reinforced by gradients in compaction pressure arising from variations in viscosity and melting rate[33]. This mechanism is in turn also controlled by the local corner flow structure and associated plate movements.

In this way surface and subsurface observations are coupled. Although the oblique, asymmetric and focused upwelling zone at the Mohns Ridge shows some of the typical characteristics for a dynamic upwelling system controlled by deep-seated pressure gradients[3,12–14], we suggest that these features could instead reflect passive upwelling controlled by asymmetric plate movements between North America and Eurasia.

Online content

Any methods, additional references, Nature Research reporting summaries, source data, statements of data availability and associated accession codes are available at https://doi.org/10.1038/s41586-019-1010-0.

Received: 3 July 2018; Accepted: 9 January 2019;
Published online 20 March 2019.

1. Dick, H. J. B., Lin, J. & Schouten, H. An ultraslow-spreading class of ocean ridge. *Nature* **426**, 405–412 (2003).
2. Evans, R. L. et al. Geophysical evidence from the MELT area for compositional controls on oceanic plates. *Nature* **437**, 249–252 (2005).
3. Forsyth, D. W. & Chave, A. D. Experiment investigates magma in the mantle beneath mid-ocean ridges. *Eos* **75**, 537–540 (1994).
4. Schlindwein, V. & Schmid, F. Mid-ocean-ridge seismicity reveals extreme types of ocean lithosphere. *Nature* **535**, 276–279 (2016).
5. Stern, T. A. et al. A seismic reflection image for the base of a tectonic plate. *Nature* **518**, 85–88 (2015).
6. Bown, J. W. & White, R. S. Variation with spreading rate of oceanic crustal thickness and geochemistry. *Earth Planet. Sci. Lett.* **121**, 435–449 (1994).
7. Reid, I. & Jackson, H. R. Oceanic spreading rate and crustal thickness. *Mar. Geophys. Res.* **5**, 165–172 (1981).
8. Zhou, H. & Dick, H. J. B. Thin crust as evidence for depleted mantle supporting the Marion Rise. *Nature* **494**, 195–200 (2013).
9. Jokat, W. et al. Geophysical evidence for reduced melt production on the Arctic ultraslow Gakkel mid-ocean ridge. *Nature* **423**, 962–965 (2003).
10. Edmonds, H. N. et al. Discovery of abundant hydrothermal venting on the ultraslow-spreading Gakkel ridge in the Arctic Ocean. *Nature* **421**, 252–256 (2003).
11. Pedersen, R. B. et al. Discovery of a black smoker vent field and vent fauna at the Arctic Mid-Ocean Ridge. *Nat. Commun.* **1**, 126 (2010).
12. Baba, K., Chave, A. D., Evans, R. L., Hirth, G. & Mackie, R. L. Mantle dynamics beneath the East Pacific Rise at 17 S: insights from the Mantle Electromagnetic and Tomography (MELT) experiment. *J. Geophys. Res. Solid Earth* **111**, B02101 (2006).
13. Key, K., Constable, S., Liu, L. & Pommier, A. Electrical image of passive mantle upwelling beneath the northern East Pacific Rise. *Nature* **495**, 499–502 (2013).
14. Wang, Y., Forsyth, D. W. & Savage, B. Convective upwelling in the mantle beneath the Gulf of California. *Nature* **462**, 499–501 (2009).
15. Cannat, M. How thick is the magmatic crust at slow spreading oceanic ridges? *J. Geophys. Res. Solid Earth* **101**, 2847–2857 (1996).
16. Michael, P. J. et al. Magmatic and amagmatic seafloor generation at the ultraslow-spreading Gakkel ridge, Arctic Ocean. *Nature* **423**, 956–961 (2003).
17. Dick, H. J. B. & Zhou, H. Ocean rises are products of variable mantle composition, temperature and focused melting. *Nat. Geosci.* **8**, 68–74 (2015).
18. Niu, Y. & Hékinian, R. Spreading-rate dependence of the extent of mantle melting beneath ocean ridges. *Nature* **385**, 326–329 (1997).
19. Su, W., Mutter, C. Z., Mutter, J. C. & Buck, R. Some theoretical predictions on the relationships among spreading rate, mantle temperature, and crustal thickness. *J. Geophys. Res. Solid Earth* **99**, 3215–3227 (1994).

20. Key, K. MARE2DEM: a 2-D inversion code for controlled-source electromagnetic and magnetotelluric data. *Geophys. J. Int.* **207**, 571–588 (2016).
21. Ni, H., Keppler, H. & Behrens, H. Electrical conductivity of hydrous basaltic melts: implications for partial melting in the upper mantle. *Contrib. Mineral. Petrol.* **162**, 637–650 (2011).
22. Constable, S. SEO3: a new model of olivine electrical conductivity. *Geophys. J. Int.* **166**, 435–437 (2006).
23. McKenzie, D., Jackson, J. & Priestley, K. Thermal structure of oceanic and continental lithosphere. *Earth Planet. Sci. Lett.* **233**, 337–349 (2005).
24. Conley, M. M. & Dunn, R. A. Seismic shear wave structure of the uppermost mantle beneath the Mohns Ridge. *Geochem. Geophys. Geosyst.* **12**, Q0AK01 (2011).
25. Bruvoll, V., Breivik, A. J., Mjelde, R. & Pedersen, R. B. Burial of the Mohn-Knipovich seafloor spreading ridge by the Bear Island Fan: time constraints on tectonic evolution from seismic stratigraphy. *Tectonics* **28**, TC4001 (2009).
26. Hermann, T. & Jokat, W. Crustal structures of the Boreas basin and the Knipovich Ridge, North Atlantic. *Geophys. J. Int.* **193**, 1399–1414 (2013).
27. Ritzmann, O., Jokat, W., Mjelde, R. & Shimamura, H. Crustal structure between the Knipovich Ridge and the Van Mijenfjorden (Svalbard). *Mar. Geophys. Res.* **23**, 379–401 (2002).
28. Hopper, J. R. et al. *Tectonostratigraphic Atlas of the North-East Atlantic Region* http://www.nagtec.org/ (Geological Survey of Denmark and Greenland, Copenhagen, 2014).
29. Baumberger, T. et al. Fluid composition of the sediment-influenced Loki's Castle vent field at the ultra-slow spreading Arctic Mid-Ocean ridge. *Geochim. Cosmochim. Acta* **187**, 156–178 (2016).
30. Spiegelman, M., McKenzie, D. J. E. & Letters, P. S. Simple 2-D models for melt extraction at mid-ocean ridges and island arcs. *Earth Planet. Sci. Lett.* **83**, 137–152 (1987).
31. Sparks, D. W., Parmentier, E. J. E. & Letters, P. S. Melt extraction from the mantle beneath spreading centers. *Earth Planet. Sci. Lett.* **105**, 368–377 (1991).
32. Gripp, A. E. & Gordon, R. G. Young tracks of hotspots and current plate velocities. *Geophys. J. Int.* **150**, 321–361 (2002).
33. Turner, A. J., Katz, R. F., Behn, M. D. & Keller, T. Magmatic focusing to mid-ocean ridges: the role of grain-size variability and non-Newtonian viscosity. *Geochem. Geophys. Geosyst.* **18**, 4342–4355 (2017).

Acknowledgements We thank the Faculty of Engineering, Department of Geoscience and Petroleum, NTNU Oceans, the ROSE consortium (with financial support from Norwegian Research Council, grant number 228400) and the Geophysics group at the Norwegian University of Science and Technology (NTNU) for funding the survey. We thank EMGS ASA for collecting excellent data in a very challenging environment.

Reviewer information *Nature* thanks Steven Constable and Rob Evans for their contribution to the peer review of this work.

Author contributions S.E.J. developed the project, analysed the data and wrote the manuscript. H.E.F.A. analysed the data and wrote the manuscript together with S.E.J. Data were processed and the Methods section was prepared by M.P. and R.M. All authors took part in data analyses, discussed the results and commented on the manuscript.

Competing interests The authors declare no competing interests.

Additional information
Extended data is available for this paper at https://doi.org/10.1038/s41586-019-1010-0.
Reprints and permissions information is available at http://www.nature.com/reprints.
Correspondence and requests for materials should be addressed to S.E.J.
Publisher's note: Springer Nature remains neutral with regard to jurisdictional claims in published maps and institutional affiliations.

METHODS

MT and CSEM data analysis and inversion. During a ten-day-long cruise, 30 broadband electromagnetic seafloor receivers were deployed along a 70-km-long line across the Mohns Ridge at Loki's Castle (Fig. 1, Extended Data Fig. 1). One of the receivers (number 23) was omitted from the processing owing to poor-quality signals. The receivers were continuously measuring the horizontal components of the electric and magnetic fields. A 281-m-long horizontal electric dipole source was towed across the receivers, emitting a time-varying electric current of 1,200 A. The source altitude above the seafloor varied strongly between 30 m and 400 m owing to safety margins in a very rough bathymetry (Extended Data Fig. 1). It was nevertheless possible to extract high-quality frequency domain CSEM data for the frequencies 0.5 Hz, 1.0 Hz, 2.0 Hz, 3.5 Hz and 9.0 Hz from the measured time series. CSEM data examples are given in Extended Data Fig. 2. For the extracted frequencies, we also obtained precise noise estimates, which are used to compute appropriate data weights in the inversion. The CSEM data have excellent quality to at least 8 km depth.

From 3–4-day-long time series, continuously registered by the seafloor electromagnetic receivers, it was possible to process high-quality MT data for periods in the range of 5.5 s to 1,500 s using robust multi-station processing[34]. MT data examples are given in Extended Data Fig. 3.

First, the electric field CSEM data were inverted using a regularized, nonlinear two-dimensional inversion with a finite element forward engine[13,20,35]. The inversion is seeking a smooth subsurface resistivity model that explains the measured data within the data uncertainty. The inversion code we used is an Occam-type inversion scheme that allows us to solve for triaxial electric anisotropy. However, we made the simplifying assumption of vertical transverse isotropy, where the resistivities in the horizontal directions are assumed to be equal and can only differ from the resistivity in the vertical direction:

$$\rho = \begin{bmatrix} \rho_x = \rho_h & 0 & 0 \\ 0 & \rho_y = \rho_h & 0 \\ 0 & 0 & \rho_z = \rho_v \end{bmatrix} \quad (1)$$

where ρ_x is the resistivity in the direction normal to the observation profile (parallel to the ridge), ρ_y is the resistivity parallel to the observation profile and ρ_z is the resistivity in the vertical direction. To stabilize the inverse problem, both smoothness and anisotropy regularization was applied, penalizing non-smooth resistivity variations and differences between the resistivity components in the horizontal and vertical directions. Consequently, the resulting resistivity model (Extended Data Fig. 4) shows strong similarities between the horizontal and the vertical resistivity. The resulting model explains the measured data with a root-mean-square misfit of 1.13, which means that the difference between the measured data and the synthetic data from the resulting resistivity model is on average 1.13 times the data uncertainty[36]. The data fit for the resulting resistivity model is shown in Extended Data Fig. 2. The start model for the non-linear inversion was a uniform half space with $\rho_v = 10\ \Omega$ m and $\rho_h = 5\ \Omega$ m, which has a root-mean-square misfit of 29.8.

Subsequently, the MT and CSEM data were inverted jointly with the same inversion code, seeking a resistivity model that explains both datasets. If three-dimensional effects are present in the data, the transverse-magnetic-mode data (ridge-perpendicular vertical current loops) are considered more reliable for two-dimensional interpretation than the transverse electric mode (ridge-parallel electric fields)[13,37,38]. Therefore, we omitted the transverse electric mode data and used only the transverse-magnetic-mode data as input to the inversion. CSEM and MT (transverse magnetic mode) data are primarily sensitive to the resistivity in the observation plane ρ_y and ρ_z. However, the inversion algorithm was not able to find a resistivity model that fulfils the vertical transverse isotropy assumption and explains the data. It was necessary to allow for triaxial anisotropy, where all diagonal elements of the resistivity tensor are free inversion parameters:

$$\rho = \begin{bmatrix} \rho_x & 0 & 0 \\ 0 & \rho_y & 0 \\ 0 & 0 & \rho_z \end{bmatrix} \quad (2)$$

In this inversion it was also necessary to apply both smoothness and anisotropy regularization to reach a stable solution. The resulting resistivity model (Extended Data Fig. 5) shows strong similarities between the resistivity components and explains the measured CSEM and MT (transverse magnetic mode) data with a root-mean-square misfit of 1.4. The start model was a homogeneous halfspace with $\rho_x = \rho_y = \rho_z = 100\ \Omega$ m with a root-mean-square misfit of 41.7. The shallow part of the joint inversion result (depth less than 10 km) is dominated by the CSEM data and shows strong similarities to the individual CSEM data inversion result (Fig. 4, Extended Data Fig. 4). Owing to the frequency-dependent attenuation of the electromagnetic signal, the deeper part of the joint inversion model is dominated by the low-frequency MT data. The MT data fit is shown in Extended Data Fig. 3. Tests confirm that the MT data in general have good sensitivity to the conductors, but below a depth of 100 km the sensitivity is relatively low.

Code availability

MARE2DEM[20] is a parallel adaptive finite element code for two-dimensional forward and inverse modelling for electromagnetic geophysics and was used for data modelling and inversion in this project. MARE2DEM is available for download at http://mare2dem.ucsd.edu/. The CSEM and MT processing software used in this study are available from EMGS ASA http://www.emgs.com/, but restrictions apply to the availability of the software, which were used under special agreement for the current study, and so they are not publicly available. The software is, however, available from the corresponding author upon reasonable request and with permission of EMGS ASA.

Data availability

The data that support the findings of this study are available from NTNU, but restrictions apply to the availability of these data, which were used under special agreement for the current study. All relevant data are, however, available from the corresponding author upon reasonable request and with the permission of NTNU.

34. Egbert, G. D. Robust multiple-station magnetotelluric data processing. *Geophys. J. Int.* **130**, 475–496 (1997).
35. Constable, S. C., Parker, R. L. & Constable, C. G. Occam's inversion: a practical algorithm for generating smooth models from electromagnetic sounding data. *Geophysics* **52**, 289–300 (1987).
36. Mittet, R. & Morten, J. P. Detection and imaging sensitivity of the marine CSEM method. *Geophysics* **77**, E411–E425 (2012).
37. Wannamaker, P. E., Hohmann, G. W. & Ward, S. H. Magnetotelluric responses of three-dimensional bodies in layered earths. *Geophysics* **49**, 1517–1533 (1984).
38. Berdichevsky, M. N. & Dmitriev, V. I. *Models and Methods of Magnetotellurics* (Springer Science & Business Media, Berlin/Heidelberg, 2010).
39. Takahashi, E. & Kushiro, I. Melting of a dry peridotite at high pressures and basalt magma genesis. *Am. Mineral.* **68**, 859–879 (1983).
40. Wyllie, P. J. Magma genesis, plate tectonics, and chemical differentiation of the Earth. *Rev. Geophys.* **26**, 370–404 (1988).
41. Maaløe, S. The solidus of harzburgite to 3 GPa pressure: the compositions of primary abyssal tholeiite. *Mineral. Petrol.* **81**, 1–17 (2004).
42. Sifré, D. et al. Electrical conductivity during incipient melting in the oceanic low-velocity zone. *Nature* **509**, 81–85 (2014).

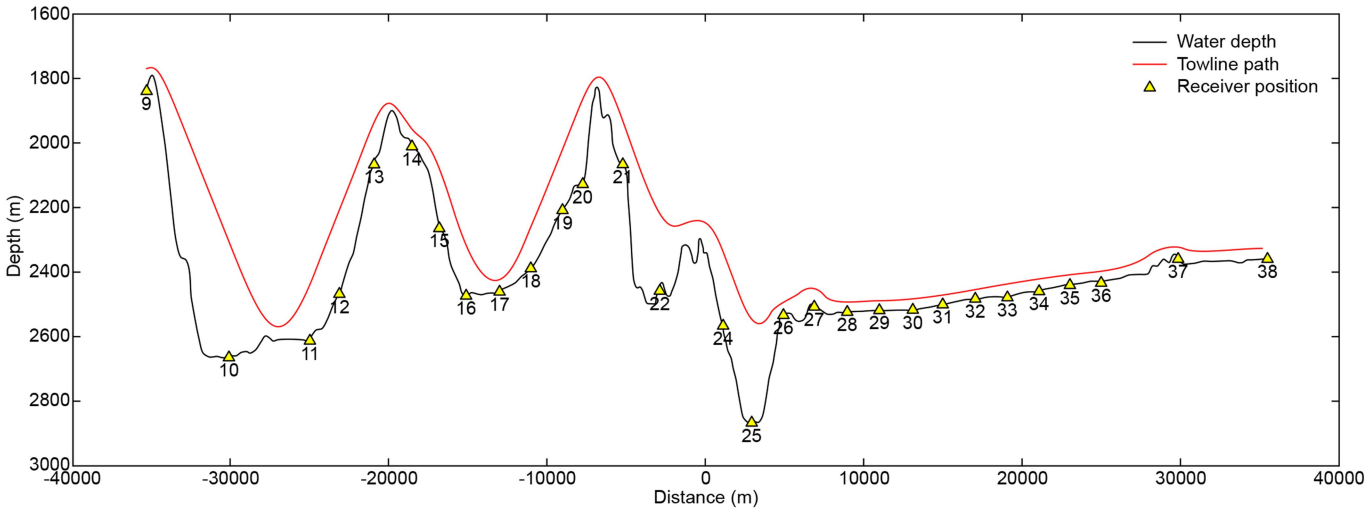

Extended Data Fig. 1 | Bathymetry and electromagnetic acquisition geometry. Water depth (black), receiver positions with names (yellow triangles) and the CSEM source track (red) for the acquired two-dimensional line at Loki's Castle.

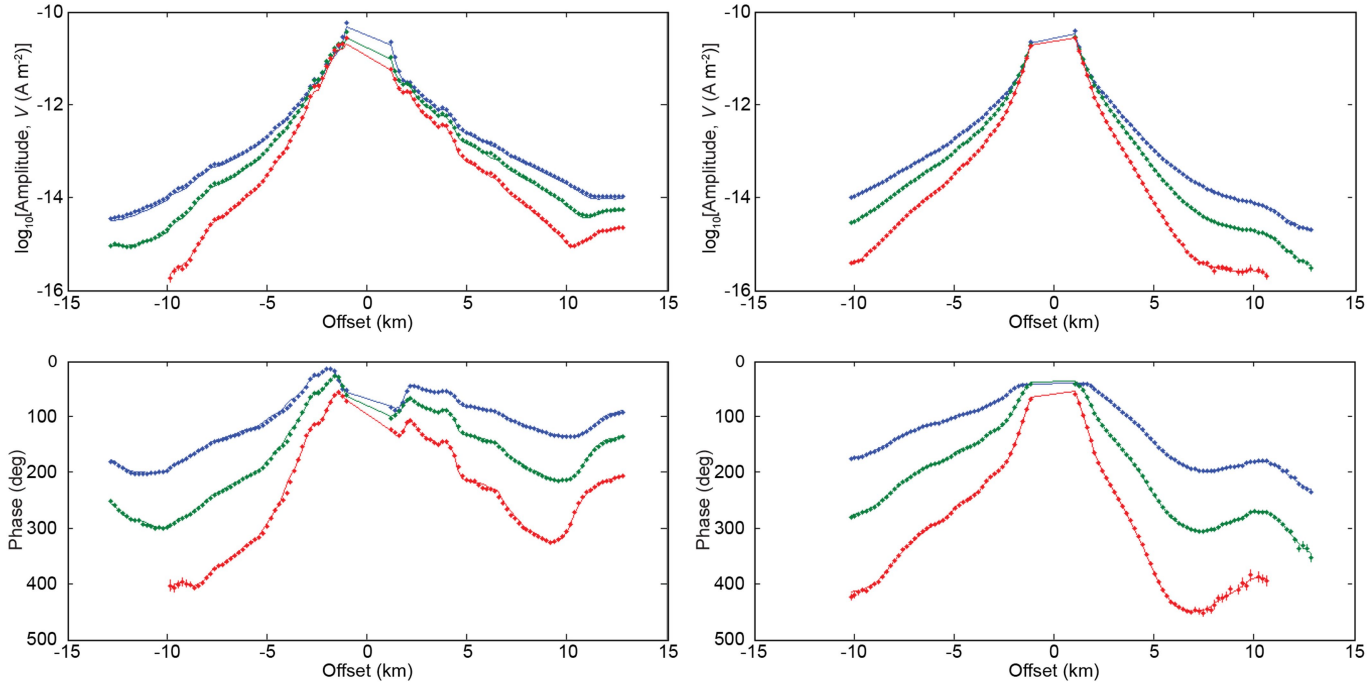

Extended Data Fig. 2 | CSEM data examples. Measured CSEM data (dots) and synthetic data for the resulting model from CSEM data inversion (lines) for two selected receivers at line positions (−3 km and +25 km). The electric-field magnitude (top) and phase data (bottom) are displayed for the frequencies 0.5 Hz (blue), 1.0 Hz (green) and 2.0 Hz (red). The total root-mean-square error for the resulting resistivity model is 1.13.

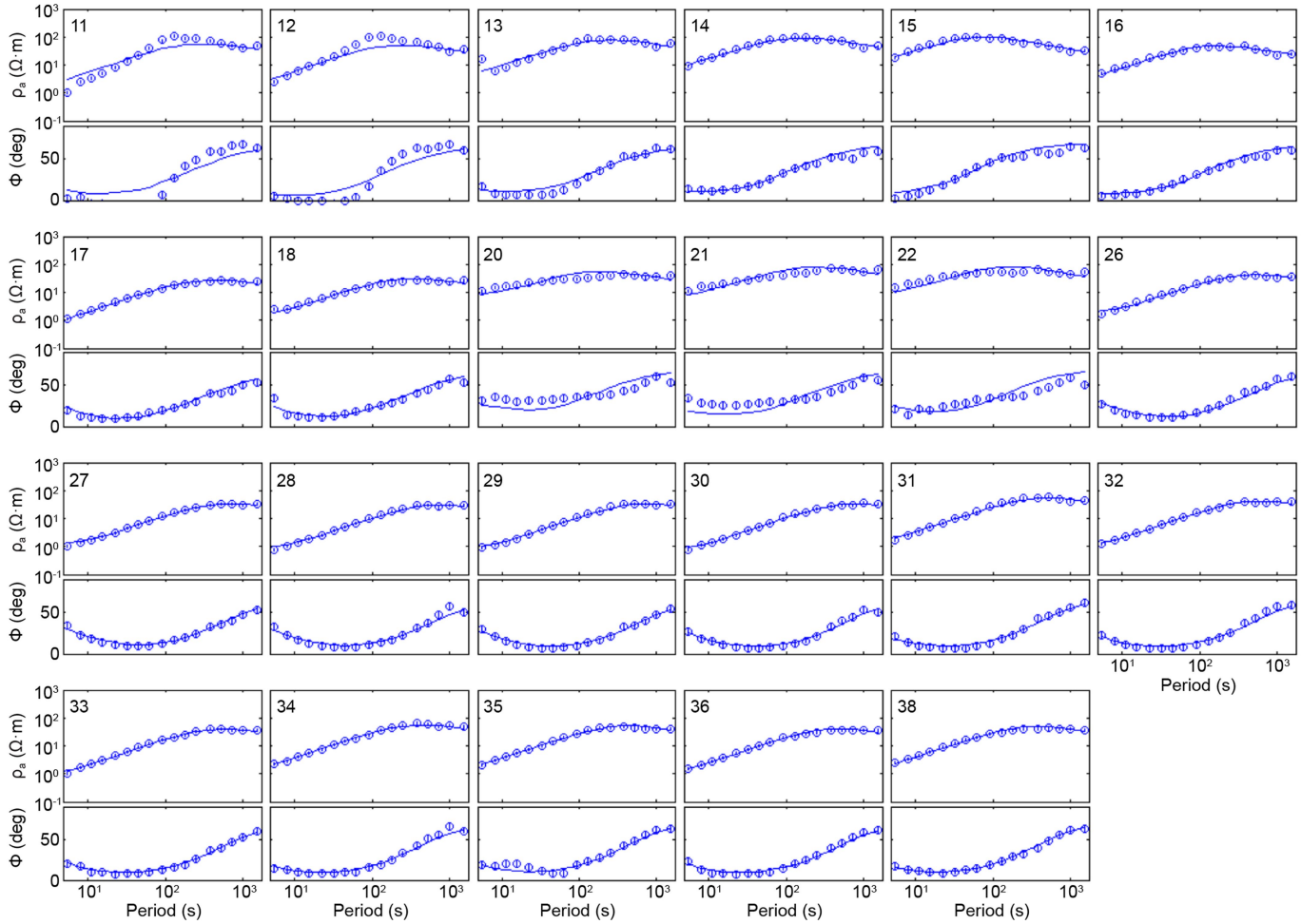

Extended Data Fig. 3 | Inverted and measured MT data. MT (transverse magnetic mode) data (circles) and synthetic data (solid lines) for the inversion result are shown for all MT stations used. The total root-mean-square misfit is 1.4. ρ_a is apparent resistivity.

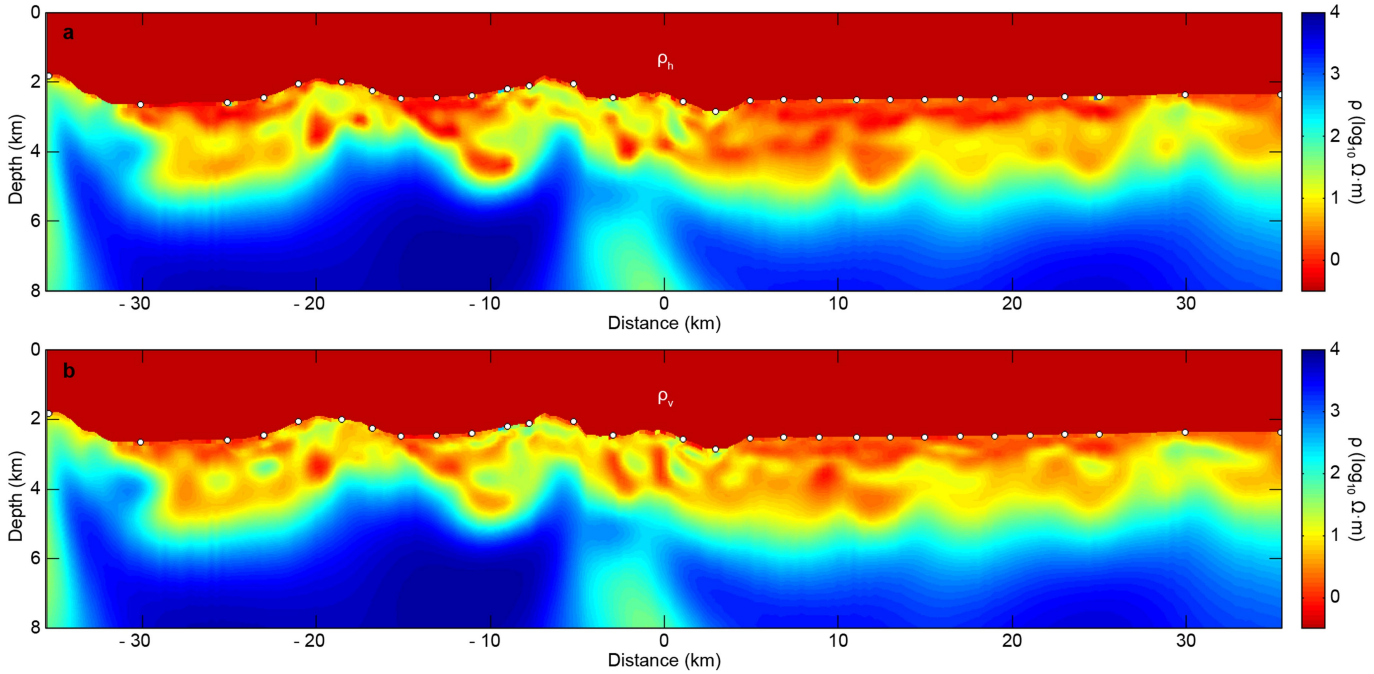

Extended Data Fig. 4 | Anisotropic resistivity model from two-dimensional CSEM data inversion. Image of the horizontal resistivity ρ_h (top) and the vertical resistivity ρ_v (bottom). The resulting model has a root-mean-square misfit of 1.13. The locations of the electromagnetic receivers are shown as white circles.

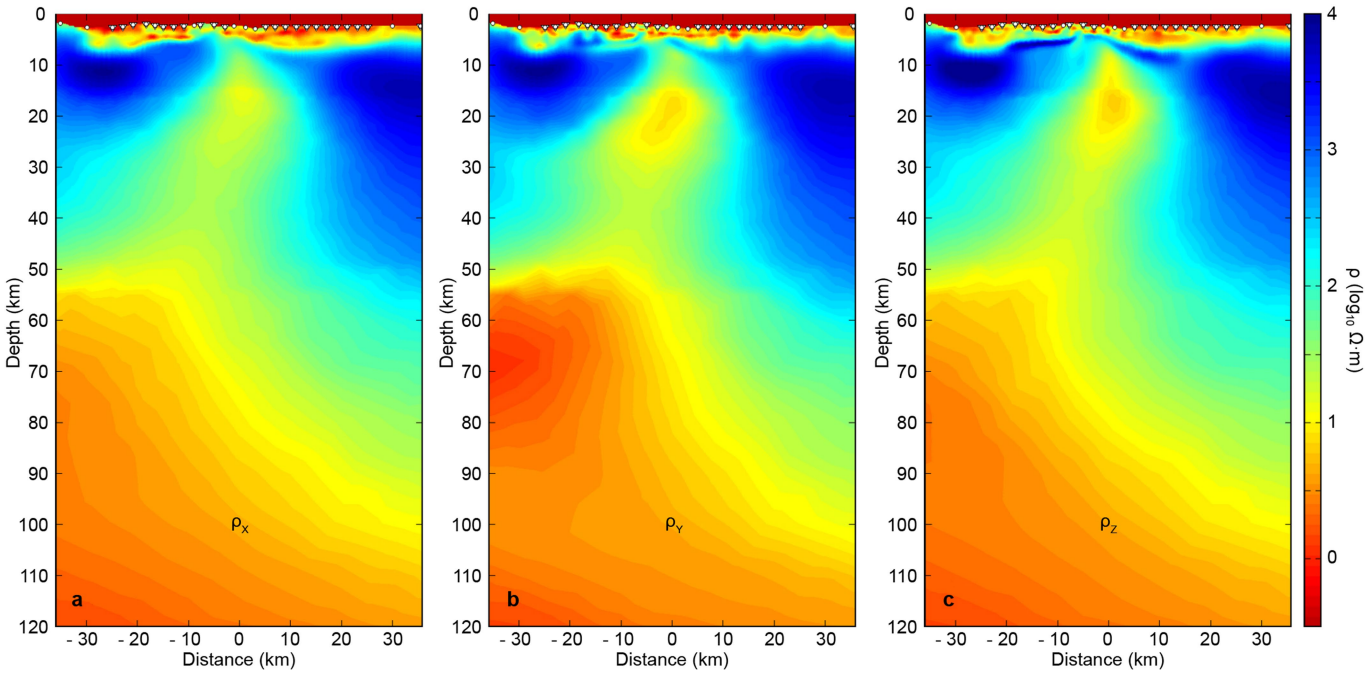

Extended Data Fig. 5 | Anisotropic resistivity model from simultaneous joint inversion of CSEM and MT (transverse magnetic mode) data. The three components of the resistivity tensor—ρ_x, ρ_y and ρ_z—show strong similarities owing to strong anisotropy regularization. CSEM receiver positions are plotted as circles, and receivers with MT used in the joint inversion are plotted as triangles. The model fits the data with a root-mean-square misfit of 1.4.

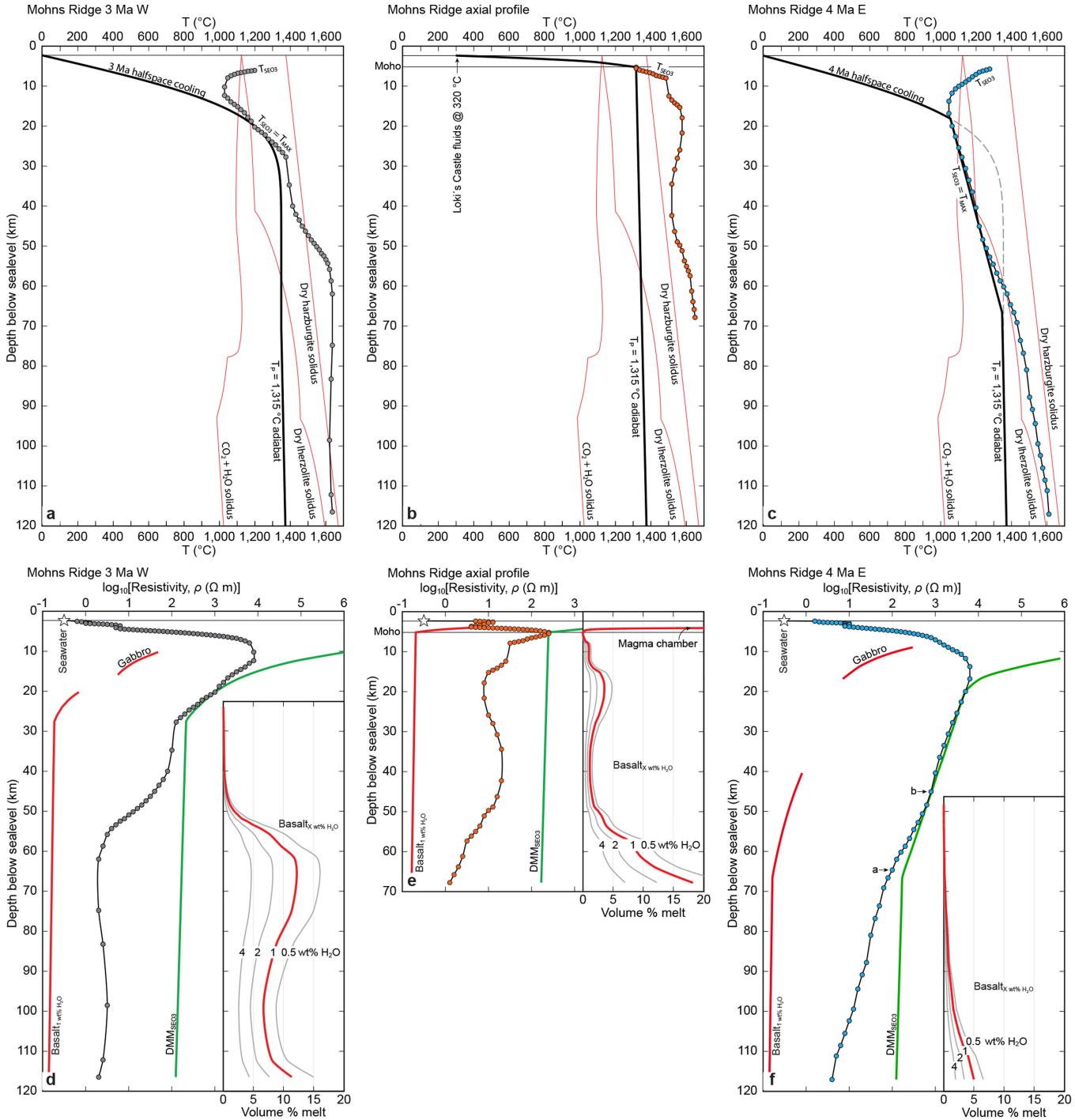

Extended Data Fig. 6 | Temperature, conductivity and melt content versus depth beneath the Mohns Ridge. a, Temperature versus depth for the 3 Myr west profile. T_{MAX}, calculated by inverting measured conductivities to T_{SEO3} (Fig. 3a), is shown as grey circles. The resulting geotherm (heavy black line) is consistent with adiabatic upwelling combined with a 3 Myr halfspace cooling model. Dry solidi for lherzolite[39,40] and harzburgite[41] are shown for reference. **b**, Temperature versus depth for the axial profile with adiabatic upwelling to the depth of the eMoho combined with a near-linear cooling trend towards 320 °C at the seabed (Loki's Castle). T_{MAX}, calculated by inverting measured conductivities to T_{SEO3} (Fig. 3a), is shown as orange circles. **c**, Temperature versus depth for the 4 Myr east profile. T_{MAX}, calculated by inverting measured conductivities to T_{SEO3} (Fig. 3a), is shown as blue circles. The resulting geotherm (heavy black line) reflects adiabatic upwelling to eLAB depth combined with a gradual cooling towards 4 Myr halfspace model temperatures about 15 km below the seabed. **d**, Resistivity versus depth and calculated melt content[42] for the 3 Myr west profile. Calculated resistivity versus depth for dry DMM (SEO3), basalt + 1 wt% H_2O and gabbro are shown for reference. **e**, Resistivity versus depth and calculated melt content[42] for the axial profile. Calculated resistivity versus depth profiles for dry DMM (SEO3), basalt + 1 wt% H_2O and gabbro are shown for reference. **f**, Resistivity versus depth and calculated melt content[42] for the 4 Myr east profile. Calculated resistivity versus depth profiles for dry DMM (SEO3), basalt + 1 wt% H_2O and gabbro are shown for reference.